ACES Asian Chemical Editorial Society

doi.org/10.1002/asia.202401477

CHEMISTRY AN ASIAN JOURNAL Research Article

www.chemasianj.org

Unravelling the Role of Sterically Encumbered Ligands in Tuning the Magnetic Properties of Lanthanide-Based D_{5h} Single-Ion Magnets

Aheli Ghatak[+],[a] Gargi Bhatt[+],[a] Rajanikanta Rana,[a] Sandeep K. Gupta,[b, c] Franc Meyer,[c] Gopalan Rajaraman,*[a] and Ramaswamy Murugavel*[a]

Isostructural Dy(III) and Er(III) complexes $[L^1{}_2Ln(H_2O)_5][I]_3 \cdot L^1{}_2 \cdot (CH_2Cl_2)$ (Ln=Dy (**1**), Er (**3**)) and $[L^2{}_2Ln(H_2O)_5][I]_3 \cdot L^2{}_2 \cdot (CH_2Cl_2)_2$ (Ln=Dy (**2**), Er (**4**)), with distorted pentagonal bipyramidal geometry (D_{5h}) around the central metal were synthesized by utilizing two bulky phosphonamide ligands, adamantyl phosphonamide, $(Ad)P(O)(NH^iPr)_2$ ($\mathbf{L^1}$) and carbazolyl phosphoramide $(Cz)P(O)(NH^iPr)_2$ ($\mathbf{L^2}$). The resultant complexes were investigated for their magnetic properties in order to elucidate the impact of modification of the coordinating P–O bond environment either by increasing steric bulk and/or introduction of a third P–N bond at the central phosphorus atom. Magnetic studies revealed substantial energy barriers (U_{eff}) of 640 K and 491 K for Dy compounds **1** and **2**, respectively, rendering them as some of the best-performing air-stable SIMs amongst the class of SIMs with D_{5h} symmetry. Compounds **1** and **2** exhibit magnetization blocking (T_B) at 6.5 K and 6 K, respectively, at a sweep rate of 20 Oe/s. Compound **1** benefits from increased lattice intermetallic distances due to bulky adamantyl substituent, but exhibits a significant deviation from linear axial (P)O–Dy–O(P) geometry (173.7(1)°). In addition to the deviation from linearity, the incorporation of a bulky adamantane (or carbazole) ligand in complex **1** (or **2**) was found to result in relatively strong Dy…H–C agostic interactions, with distances of 3.698 Å (3.376 Å). These interactions are expected to induce transverse anisotropy. Ab initio CASSCF/RASSI-SO/SINGLE_ANISO calculations offer valuable insights into the dynamics of magnetic relaxation and the impact of axial bulkiness on the anisotropy of D_{5h} systems. Beyond highlighting the crucial role of crystal field and symmetry in achieving high-temperature SIMs, this study also explores how the secondary coordination sphere can be engineered to create novel SIMs.

Introduction

Traditional magnetic storage devices employ magnetic domains to retain electronic data. However, the exponential growth of data necessitates a more compact storage solution.[1] While the "top-down" approach has enhanced storage density through miniaturization, further reduction in device size compromises efficiency due to inter-domain interactions. This is where molecular magnetism comes into play. Single-molecule magnets (SMMs) exhibit magnetic bistability and blockade of permanent magnetization below a certain temperature called blocking temperature (T_B).[2–5] These molecules can potentially decrease the size of a 'bit' to a molecular level, facilitating high-density data storage.[6] Furthermore, SMMs exhibit quantum phenomena such as quantum tunnelling of magnetization (QTM) and quantum phase interference, thus making them promising candidates for future molecular spintronics and quantum computing.[7–10] However, the realization of their full potential is currently impeded by the necessity of low temperatures to observe these quantum effects.

Various researcher groups have aimed at enhancing the operational temperature of single-molecule magnets (SMMs) through precise modulation of molecular symmetry and anisotropy. While the discovery of slow magnetic relaxation in molecular complexes was achieved with a Mn_{12} cluster,[5,11] the subsequent realization of exceptionally high energy barriers (U_{eff}) in double-decker complexes $[Pc_2Tb][TBA]$ in 2003[12] redirected the interest towards lanthanide-based systems for the development of advanced single-molecule magnets.[13–23] Among the lanthanides, Dy(III) complexes have emerged as prime candidates due to their large ground-state magnetic moment and pronounced spin-orbit coupling, which collectively contribute to elevated energy barriers (U_{eff}) for magnetization reversal.[24–27] Achieving substantial blocking temperatures in dysprosium-based SIMs necessitates the maximization of the easy-axis anisotropy in the system, often realized through the employment of axial ligands that complement Dy(III) ion's oblate electronic distribution.[26,28] The introduction of bulky ligands was earlier proposed to diminish metal-metal interactions by enhancing the intermetallic distance, thereby increas-

[a] A. Ghatak,[+] G. Bhatt,[+] R. Rana, G. Rajaraman, R. Murugavel
Department of Chemistry, Indian Institute of Technology, Bombay, Powai, 400076 Mumbai, India
E-mail: rajaraman@chem.iitb.ac.in
rmv@chem.iitb.ac.in

[b] S. K. Gupta
Department of Chemistry, Indian Institute of Technology, Delhi, Hauz Khas, 110016 New Delhi, India

[c] S. K. Gupta, F. Meyer
University of Göttingen, Institute of Inorganic Chemistry, D-37077 Göttingen, Germany

[+] Contributed equally

Supporting information for this article is available on the WWW under https://doi.org/10.1002/asia.202401477

ing the energy gap between ground and excited states. Theoretical calculations on perfectly linear molecules containing dysprosium(III) ion, e.g. $[Dy{=}O]^{+}$, indicated extraordinarily high energy barriers.[29–30] While pseudo-two-coordinate lanthanide-based complexes with elevated blocking temperatures have been extensively studied,[27,31–33] recent experimental investigations on a two-coordinate Dy(III) compound have revealed significantly lower energy barriers compared to the predicted value.[34] This discrepancy is attributed to the non-linear structure of the molecule as well as vibrations originating from the ligand atoms coordinated to the dysprosium ion, which enhances the spin-phonon coupling.

In 2017, Goodwin et al. reported the dysprosocenium complex $[Dy(Cp^{ttt})_2][B(C_6F_5)_4]$, (where Cp^{ttt} = 1,2,4-tri-*tert*-butylcyclopentadienyl), which exhibited hysteresis at temperatures up to 60 K at a sweep rate of 22 Oe/s.[26] This record was subsequently surpassed by Guo et al., who reported a blocking temperature of 80 K for the pseudo-linear compound $[(\eta^5\text{–}Cp^*)Dy(\eta^5\text{–}Cp^{i}Pr_5)][B(C_6F_5)_4]$.[35] A similar blocking temperature has also been reported by Gould *et al.* for mixed-valence dilanthanide complex $[Dy_2I_3(Cp^{i}Pr_5)_2]$ with metal-metal bonding in 2022.[36] However, similar to most of the other compounds exhibiting pronounced energy barriers and blocking temperatures, this complex suffers from lack of air stability, a critical limitation for practical applications in this domain. Circumventing this challenge, we had earlier reported an air-stable Dy(III) single-ion magnet (SIM) $[L_2Dy(H_2O)_5][I]_3\cdot L_2\cdot(H_2O)$ (**A**) where $L = (^{t}BuPO(NH^{i}Pr)_2)$].[37] This complex with a pseudo-D_{5h} symmetry exhibited a blocking temperature of 12 K and a substantial anisotropy barrier (U_{eff}) of 735.4 K, significant coercivity and exceptional atmospheric resistance. A comparative table of D_{5h} air-stable Dy-based D_{5h} complexes highlighting pronounced blocking temperatures and energy barriers is given in Table 1.

Continuing our studies on axially coordinated single-ion-magnets, we report here two sets of air-stable Dy and Er-based Ln(III) SIMs with pseudo D_{5h} symmetry, unraveling the role of well-designed sterically encumbered phosphon(r)amide ligands $(Ad)P(O)(NH^{i}Pr)_2$ ($\mathbf{L^1}$) and $(Cz)P(O)(NH^{i}Pr)_2$ ($\mathbf{L^2}$) in fine-tuning the magnetic properties of D_{5h} complexes. Additionally, this study explores the impact of using a phosphoramide compared to a phosphonamide, in conjunction with steric factors, and additional Dy…H–C agostic interactions on the overall behaviour. Compounds **1** and **2** exhibit well-separated Dy(III) centres within the lattice and demonstrate relatively high anisotropic barriers with substantial blocking temperatures in comparison to previously reported air-stable 4f systems, $[L_2Dy(H_2O)_5][I]_3\cdot L_2\cdot(H_2O)$ (**A**).

Results and Discussion

Synthesis of $(Ad)P(O)(NH^{i}Pr)_2$ ($\mathbf{L^1}$) and $(Cz)P(O)(NH^{i}Pr)_2$ ($\mathbf{L^2}$)

$(Ad)P(O)(NH^{i}Pr)_2$ ($\mathbf{L^1}$) and $(Cz)P(O)(NH^{i}Pr)_2$ ($\mathbf{L^2}$) have been synthesized to explore the effect of substituents on the phosphoryl moiety, which can therefore influence the SIM properties of D_{5h} systems. The precursor for $\mathbf{L^1}$, adamantyl phosphonic dichloride ($(Ad)P(O)Cl_2$), was initially synthesized from the reaction of adamantyl bromide, PCl_3, and $AlCl_3$ following a reported procedure.[38] Amination of this dichloride in toluene in the presence of excess isopropyl amine under a nitrogen atmosphere leads to the formation of $\mathbf{L^1}$. For $\mathbf{L^2}$, the intermediate product carbazolyl phosphonyl dichloride ($(Cz)P(O)(Cl)_2$) is prepared by the in-situ reaction of lithium carbazol-9-ide with $POCl_3$ which is further reacted with an excess of isopropyl amine to obtain $\mathbf{L^2}$ (Scheme 1).

The formation of the products has been confirmed with the help of ^{31}P NMR spectroscopy, which shows a single resonance at δ 31.89 ppm for $\mathbf{L^1}$ and δ 4.91 ppm for $\mathbf{L^2}$ (Figures S1 and S2). The chemical shift observed for $\mathbf{L^1}$ is consistent with those reported for phosphonamides.[39] The considerable upfield shift in $\mathbf{L^2}$ with respect to $\mathbf{L^1}$ garners evidence of an altered environment around the phosphorous atom in $\mathbf{L^2}$ owing to the

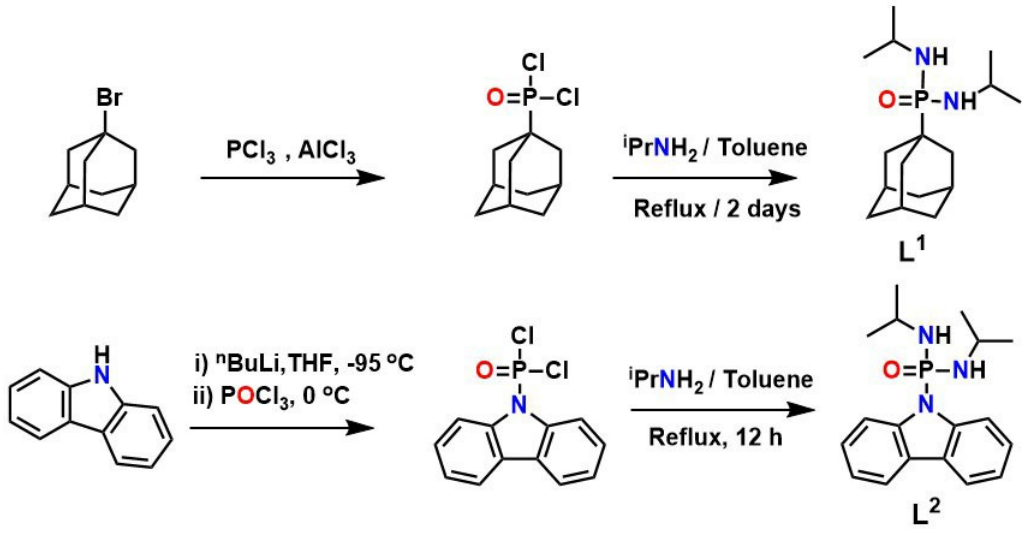

Scheme 1. Synthesis of $\mathbf{L^1}$ and $\mathbf{L^2}$.

Table 1. Dy(III) based single-ion magnets ($U_{eff,ac}$ represents the barrier obtained from ac susceptibility measurements, $U_{eff,cal}$ represents the barrier obtained from computational studies, and C and n are the parameters obtained from the fitting of the temperature dependence of relaxation time corresponding to the Raman process).

Sl No.	Dy-D_{5h} SIMs	Trans O–P–O angle [°]	FC/ZFC T_B [K]	Orbach			Raman		QTM_{cal} [s]	Relaxation from KD	Ref
				U_{effrac} [K]	τ_0 ($\times10^{-11}$) [s]	$U_{effrcal}$ [K]	C s^{-1} K^{-n}	n			
1	$[L^1{}_2Dy(H_2O)_5][I]_3.L^1{}_2.CH_2Cl_2$ (**1**)	173.7(1)	6.5	640	0.795	667	8.88×10^{-5}	3.77	1.7×10^{-5}	3rd	This work
2	$[L^2{}_2Dy(H_2O)_5][I]_3L^2{}_2.(CH_2Cl_2)_2$ (**2**)	169.3(1)	6	491	0.0132	571	2.27 x 10^{-4}	5.13	2.7×10^{-4}	3rd	This work
3	$[L_2Dy(H_2O)_5][I]_3.L_2.H_2O$ (**A**)	175.14(9)	12	651	0.563	668	6.92×10^{-4}	3	1.3×10^{-5}	3rd	[37]
4	$[L_2Dy(H_2O)_5][Cl]_3.L_2.H_2O$	172.19(6)	8.2	609	0.66	606.3	2.0×10^{-4}	3.6	7.0×10^{-6}	3rd	[60]
5	$[L_2Dy(H_2O)_5][Br]_3.L_2.H_2O$	177.68(8)	11.6	640	1.1	645.7	7.2×10^{-7}	4.7	7.4×10^{-6}	3rd	[60]
6	$[(Cy_3PO)_2Dy(H_2O)_5][Cl]_3\cdot(Cy_3PO)\cdot H_2O\cdot EtOH$	175.8(1)	8	472	0.87	418		5.7	3.7×10^{-4}	3rd	[61]
7	$[(Cy_3PO)_2Dy(H_2O)_5]Br_3\cdot(Cy_3PO)_2\cdot2H_2O\cdot2EtOH$	179.0(1)	11	543	2.0	529		5.6	1.1×10^{-4}	4th	[61]
8	$[(CyPh_2PO)_2Dy(H_2O)_5][Br]_3\cdot(CyPh_2PO)_2\cdot EtOH\cdot(H_2O)_3$	174.2(2)	11	508	0.86	450		4.0	7.1×10^{-4}	2nd	[62]
9	$[(HMPA)_2Dy(H_2O)_5][Cl]_3\cdot HMPA\cdot H_2O$	175.58(6)	7	460	2.0	572			1.3×10^{-5}	3rd	[63]
10	$[(HMPA)_2Dy(H_2O)_5][I]_3\cdot(HMPA)_2$	177.9(1)	8	600	1.2	622			9.6×10^{-6}	3rd	[63]
11	$[(Cy_3PO)_2Dy(H_2O)_5](CF_3SO_3)_3\cdot(Cy_3PO)_2$	173.42	8.5	562	1.7	732			7.5×10^{-5}	3rd	[64]
12	$[(Cl)_2Dy(THF)_5][BPh_4]$ *(field-induced)*	176.64(4) 179.31(5)	–	75.6	83.1	58.8				3rd	[49]
13	$[(OCMe_3)(Cl)Dy(THF)_5][BPh_4]$	178.26(9)	7.0	912.8	0.43	786.8	1.7×10^{-6}	4.5	–	3rd	[49]
14	$[(OSiMe_3)(Cl)Dy(THF)_5][BPh_4]$	178.50(7)	4.5	780	2.81	785.4	6.45×10^{-6}	4.2	–	3rd	[49]
15	$[(OCMe_3)(Br)Dy(THF)_5][BPh_4]$	178.0(1)	4.5	819	1.69	803	4.46×10^{-5}	3.7	–	3rd	[49]
16	$[(OSiMe_3)(Br)Dy(THF)_5][BPh_4]$	178.95(6)	4.5	733	1.07	681.2	6.60×10^{-6}	4.5	–	3rd	[49]
17	$[(OPh)(Cl)Dy(THF)_5]$ $[BPh_4]$	178.5(1)	6.8	737.3	4.46	585.6	1.51×10^{-5}	4.1	–	3rd	[49]
18	$[Na(THF)_5][(OPh)_2Dy(THF)_5]$ $[BPh_4]_2$	176.3(1)	12.0	1330.6	0.49	1228.3	1.02×10^{-6}	4.0	–	4th	[49]

ACES Asian Chemical Editorial Society
CHEMISTRY AN ASIAN JOURNAL Research Article

presence of the third P–N bond.[40] Additional evidence for the purity of the synthesized ligands has been obtained from ^{1}H and ^{13}C NMR spectroscopy as well as through mass spectrometry and infrared spectroscopy (Figures S3–S10).

Molecular Structure of (Cz)P(O)(NH^{i}Pr)$_2$ (L^2)

Ligand L^2 was isolated as colourless block crystals from methanol at ambient conditions. It crystallizes in the orthorhombic space group *Pna*2$_1$. There are two molecules of phosphonic triamide in the asymmetric part of the unit cell (Figure 1a) which are linked via intermolecular H-bonding (Figure 1b). The details for bond lengths and bond angles are given in Table S1. The presence of a non-crystallographic mirror symmetry running through the P=O axis in L^2 imposes the participation of both the N–H groups in hydrogen bonding (Table S2), thus forming six-membered PN_2H_2O rings along the polymeric chain. However, no inter-chain hydrogen bonds are observed. The observed P=O and P–N distances are consistent with the expected values for these linkages.[39]

Synthesis of $[L^1{}_2Ln(H_2O)_5][I]_3\cdot L^1{}_2\cdot(CH_2Cl_2)$ [Ln = Dy (1), Er (3)] and $[L^2{}_2Ln(H_2O)_5][I]_3\cdot L^2{}_2\cdot(CH_2Cl_2)_2$ [Ln = Dy (2), Er (4)]

Seven-coordinated monometallic Ln(III) cationic complexes **1**–**4** were synthesized utilizing bulky phosphon(r)amide ligands L^1 and L^2 and corresponding hydrated lanthanide iodides. The synthetic procedure involves a reaction between $LnI_3.xH_2O$ (Ln=Dy/Er) and the phosphon(r)amide ligand L^1 in a 1:2 molar ratio (for **1** and **3**) or L^2 in a 1:4 molar ratio (for **2** and **4**) in dichloromethane (Scheme 2). The reaction mixture was heated under reflux for 6 h before cooled down to room temperature. The clear yellow solution was filtered and left undisturbed at ambient aerobic conditions for crystallization. Slow evaporation of dichloromethane resulted in the isolation of yellow block-shaped single crystals with general formula $[L^1{}_2Ln(H_2O)_5][I]_3\cdot L^1{}_2\cdot(CH_2Cl_2)$ [Ln=Dy(**1**), Er(**3**)] and $[L^2{}_2Ln(H_2O)_5][I]_3\cdot L^2{}_2\cdot(CH_2Cl_2)_2$ [Ln=Dy (**2**), Er (**4**)]. All the compounds are stable in the presence of air or moisture for extended periods.

The infrared spectra of compounds **1**–**4** show broad peaks centered at 3316 cm^{-1} for **1**, 3299 cm^{-1} for **2**, 3291 cm^{-1} for **3**, and 3303 cm^{-1} for **4** which can be attributed to the merging of O–H stretching frequency of the coordinated water molecules with the N–H stretching band of the phosphon(r)amide ligands (Figure S11). The C–H stretching vibrations of the alkyl groups are observed in the range of 2870 cm^{-1} to 2931 cm^{-1}. Further, the peaks at 1421 cm^{-1} for **1**, 1424 cm^{-1} for **2**, 1423 cm^{-1} for **3** and 1428 cm^{-1} for **4** correspond to C–N stretching frequencies. The characteristic P=O absorption frequency for complexes **1**–**4** has been observed at around 1100–1131 cm^{-1} which are shifted to lower wavenumbers compared to the respective ligands (1223 cm^{-1} (L^1) and 1204 cm^{-1} (L^2)), and are consistent with the P–O bond elongation due to Ln–O bond formation.

Molecular Structures of Complexes 1–4

Single crystal X-ray diffraction studies of the block-shaped crystals reveal that the compounds **1** and **3** are isostructural and crystallize in orthorhombic space group *Aea*2 while **2** and **4** are also isostructural crystallizing in orthorhombic space group *I*2/a. While the space group is different due to variations in the ligand system, the core structures of compounds **1**–**4** are similar. The molecular structure as depicted in Figure 2 reveals a

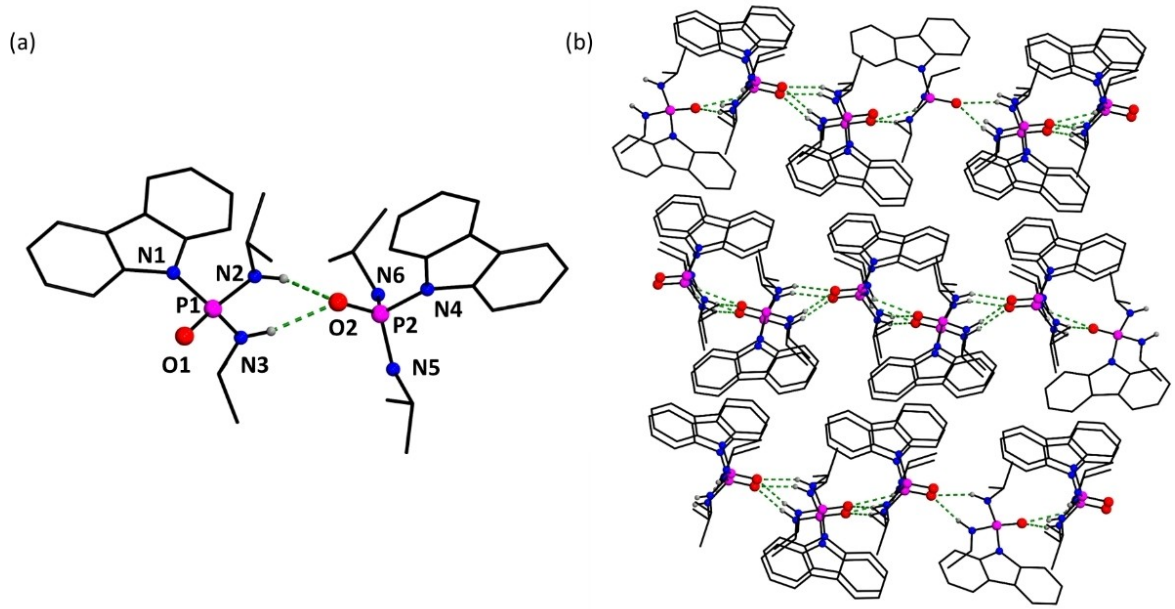

Figure 1. (a) Molecular structure of L^2 and (b) packing diagram down b axis.

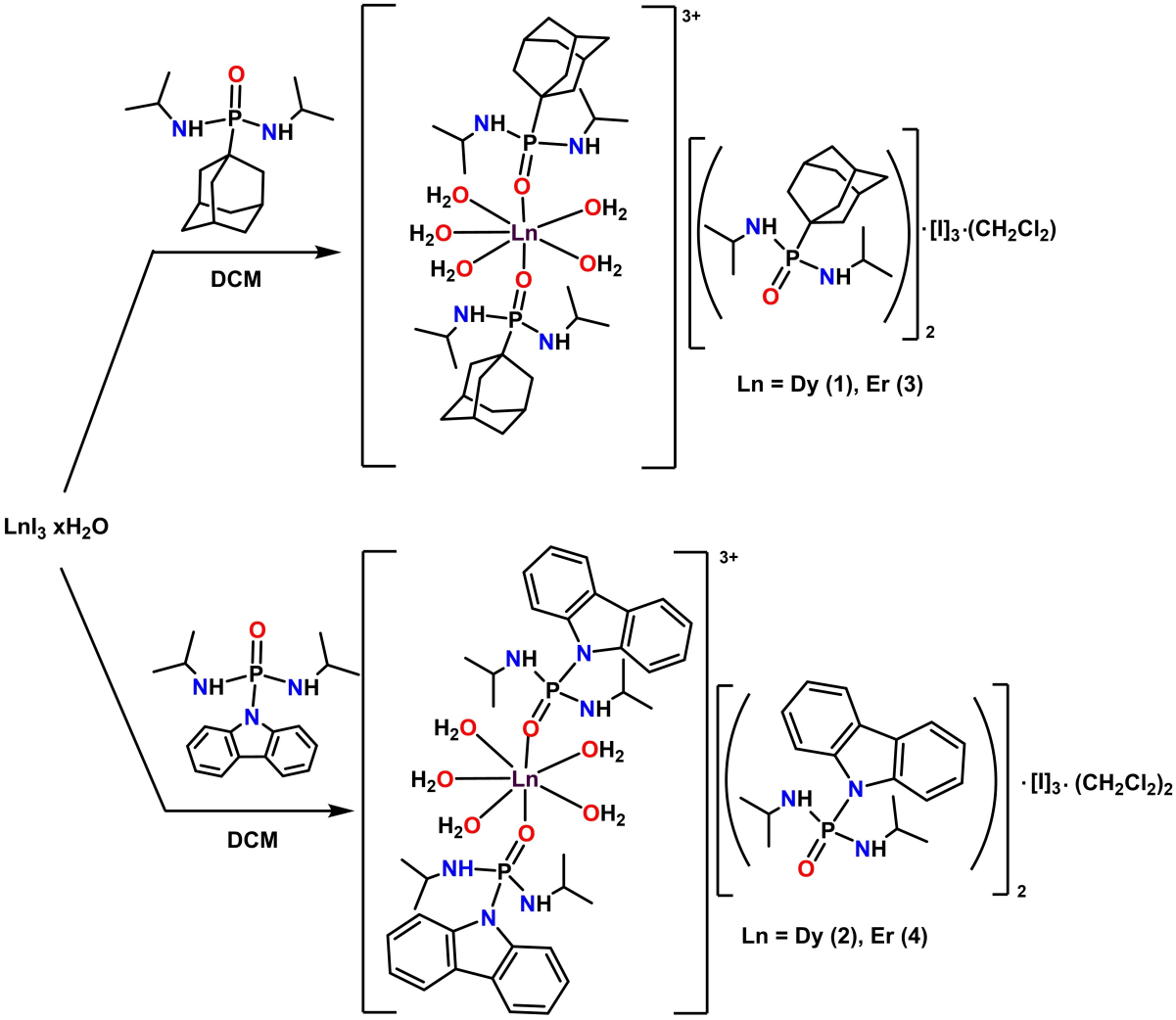

Scheme 2. Synthesis of monometallic Ln(III) complexes **1**–**4**.

seven-coordinate Ln(III) ion in a pseudo-D_{5h} symmetry where the central lanthanide ion is bonded to two phosphon(r)amide moieties (L^1 or L^2) through the oxygen atoms of the phosphoryl groups (P=O) which occupy the axial positions of the pentagonal bipyramidal geometry. This is evident from the increased P–O bond lengths in compounds **2** (1.505(2) Å) and **4** (1.501(3) Å), compared to the ligand L^2 (1.476(3) Å), as determined from their crystal structures. Five water molecules occupy the equatorial coordination sites around the central lanthanide ion. The average Dy–O(aqua) distance in the equatorial plane is 2.375 Å for **1** and 2.360 Å for **2**, which are significantly longer than Dy–O(P) axial distances (2.194(3) Å (**1**) and 2.221(2) Å (**2**)). This signifies a stronger bonding of the phosphon(r)amide with the Dy(III) ion compared to the equatorially coordinated water molecules. The axial O(P)–Dy–O(P) angle of 173.7(1)° (**1**) and 169.3(1)° (**2**) (Figure 3) and the average cis O(W)–Dy–O(W) angle of 72.1° (**1**) and 71.7° (**2**) indicate a nearly ideal pentagonal bipyramidal geometry around the central metal ion. Apart from the two axial ligands, two more phosphon(r)amide units (one from the current unit cell and another from the next unit cell) are bound to the equatorial water molecules via intramolecular H-bonding interactions forming an extended structure. This leads to the increased intermetallic distance between two neighbouring Dy(III) centers, which is 14.28 Å (**1**) and 11.94 Å (**2**), similar to those observed in earlier reported D_{5h} Ln-complexes.[37,41–42] The non-coordinating iodide ions are present in the secondary coordination sphere of the crystal lattice which maintains the electroneutrality of the compounds. These iodide ions are held together with the lanthanide ion via H-bonds mediated through metal-bound water molecules. Bond lengths, bond angles and H-bonding are listed in Tables S4–S7.

Compounds **3** and **4** exhibit structural features and hydrogen bonding patterns analogous to their Dy(III) counterparts (Tables S8–S11). The Er–O(P) axial bond length in compound **3** is 2.183(4) Å and the trans axial bond angle O1–Er–O1 is 173.9(3)°. This suggests that the axial ligation is more linear for the Er(III) complex compared to **1**. In contrast, complex **4** displays a further deviation from ideal geometry with an axial bond angle of 168.6(1)°. The corresponding bond length of

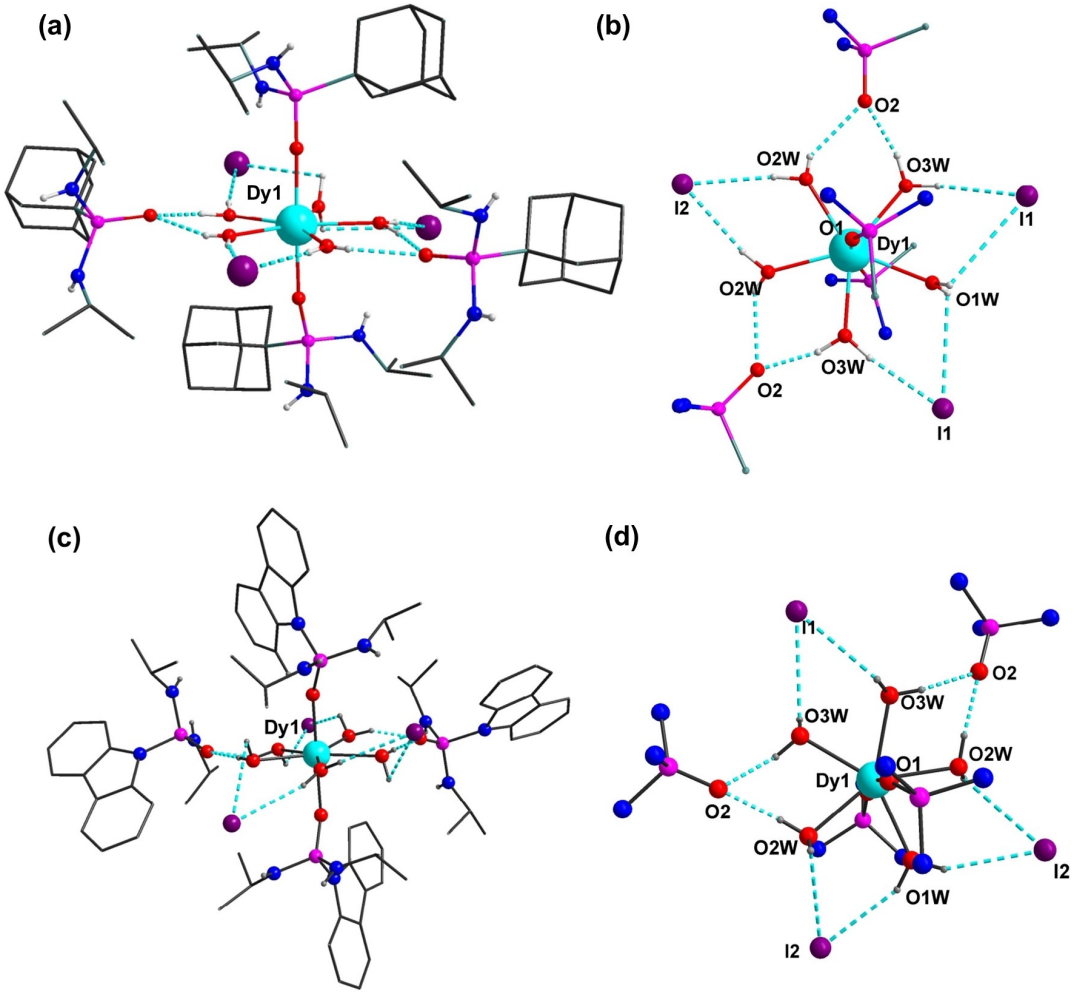

Figure 2. (a, c) Molecular structure of **1** and **2**. Lattice dichloromethane molecules and H-atoms attached to the carbon atoms have been omitted for clarity. The H-atoms of the water molecules are hydrogen bonded to the three iodide anions and two lattice phosphonic diamide ligands. (b, d) A star-shaped hydrogen bonding pattern in **1** and **2**.

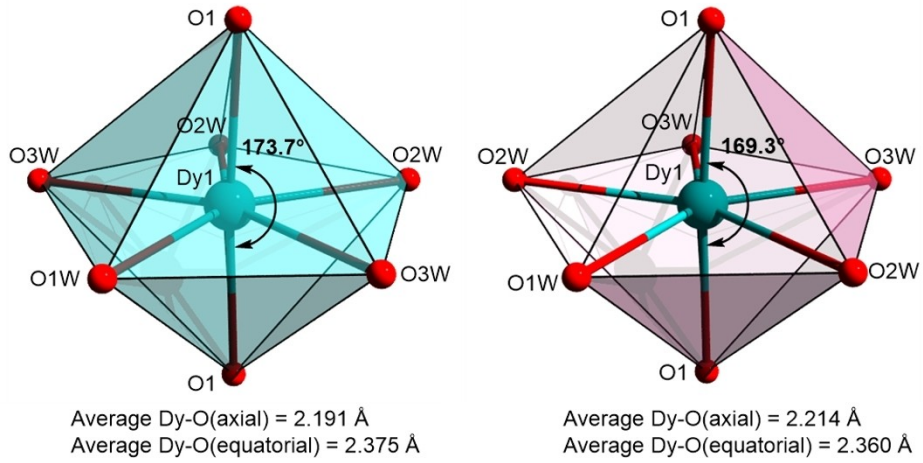

Figure 3. Polyhedral view and comparison of the deviation from ideal pentagonal-bipyramid coordination environment around Dy(III) ion in **1** and **2**.

2.215(3) Å is comparable to that observed in complex **2**. In both the complexes, the equatorial Er–O(W) distance lies in the range 2.304–2.355 Å, indicating longer equatorial bonds than axial.

In the core structures of **1**–**4**, the central lanthanide ions are coordinated to seven oxygen atoms, five from water molecules and two from phosphon(r)amide oxygen atoms. The least

deviation from the ideal seven-coordinate geometries for the [LnO_7] core, analyzed using SHAPE2.1 software,[43] reveals a distorted pentagonal bipyramidal geometry around the central metal ion. The deviation from the ideal geometries is shown in Table S12. Bulk purity of the **1**–**4** samples was ensured from the powder X-ray diffraction analyses (Figures S12–S15) and elemental analyses.

Magnetic Studies

The direct current (dc) susceptibility measurements on polycrystalline samples **1** and **2**, carried out in the temperature range 2–200 K in an applied field of 0.5 T, show $\chi_M T$ values of 13.67 and 13.99 $cm^3 K mol^{-1}$, respectively, at 200 K (Figure 4). These values are close to the expected value of 14.18 $cm^3 K mol^{-1}$ for an isolated Dy(III) ion (ground state $= {}^6H_{15/2}$). On cooling, the $\chi_M T$ value gradually decreases to a value of 11.83 $cm^3 K mol^{-1}$ for **1** and 10.20 $cm^3 K mol^{-1}$ for **2** until 8 K before steeply decreasing to 5.93 and 6.5 $cm^3 K mol^{-1}$, respectively, at 2.0 K which is indicative of the presence of magnetic blocking. The field-dependent magnetization curves for both **1** and **2** show a steep increase in magnetization (4.78 and 4.67 μ_B, respectively) until 2 T, gradually reaching the values of 5.0 μ_B for **1** and 5.4 μ_B for **2** at 7.0 T (Figures S16b and S17b). This can be attributed to the existence of strong easy-axis magnetic anisotropy for both complexes.

Complexes **3** and **4** show $\chi_M T$ values of 11.69 and 11.44 $cm^3 K mol^{-1}$, respectively, at 200 K (Figure 4) which are close to that expected for an isolated Er(III) ion with a ground state of ${}^4I_{15/2}$ (11.48 $cm^3 K mol^{-1}$). Upon cooling the compound **3**, the value remains almost unchanged till ~100 K. Further lowering the temperature causes a gradual decrease in $\chi_M T$ value to 10.98 $cm^3 K mol^{-1}$ at 65 K followed by a sharp decrease in $\chi_M T$ value to 5.21 $cm^3 K mol^{-1}$ at 2.0 K. However, in **4**, the $\chi_M T$ value remains constant upon cooling up to 125 K followed by a decrease to 6.9 $cm^3 K mol^{-1}$ at 8.0 K before steeply decreasing to 4.5 $cm^3 K mol^{-1}$ at 2.0 K. The variable field magnetization curves for both **3** and **4** show a sharp increase to 3.54 μ_B (**3**) and 2.6 μ_B (**4**) at 1 T followed by a gradual increase to 5.61 μ_B and 5.4 μ_B, respectively, at 7 T with no clear saturation.

The relaxation dynamics of magnetization in **1**–**4** have been explored with the help of alternating current (ac) susceptibility measurements with an oscillating field of 3.5 Oe. A well-defined maximum in the frequency-dependent out-of-phase component of ac susceptibility (χ_M'') is observed between 0.2 and 969 Hz at zero applied dc field for both compounds **1** and **2**. This maximum can be observed in the temperature range of 4–37 K for **1** and 5–26 K for **2** (Figures 5b and 6b). Fitting of the relaxation time using multiple relaxation processes as shown in equation (1) over the whole range of temperature yields an

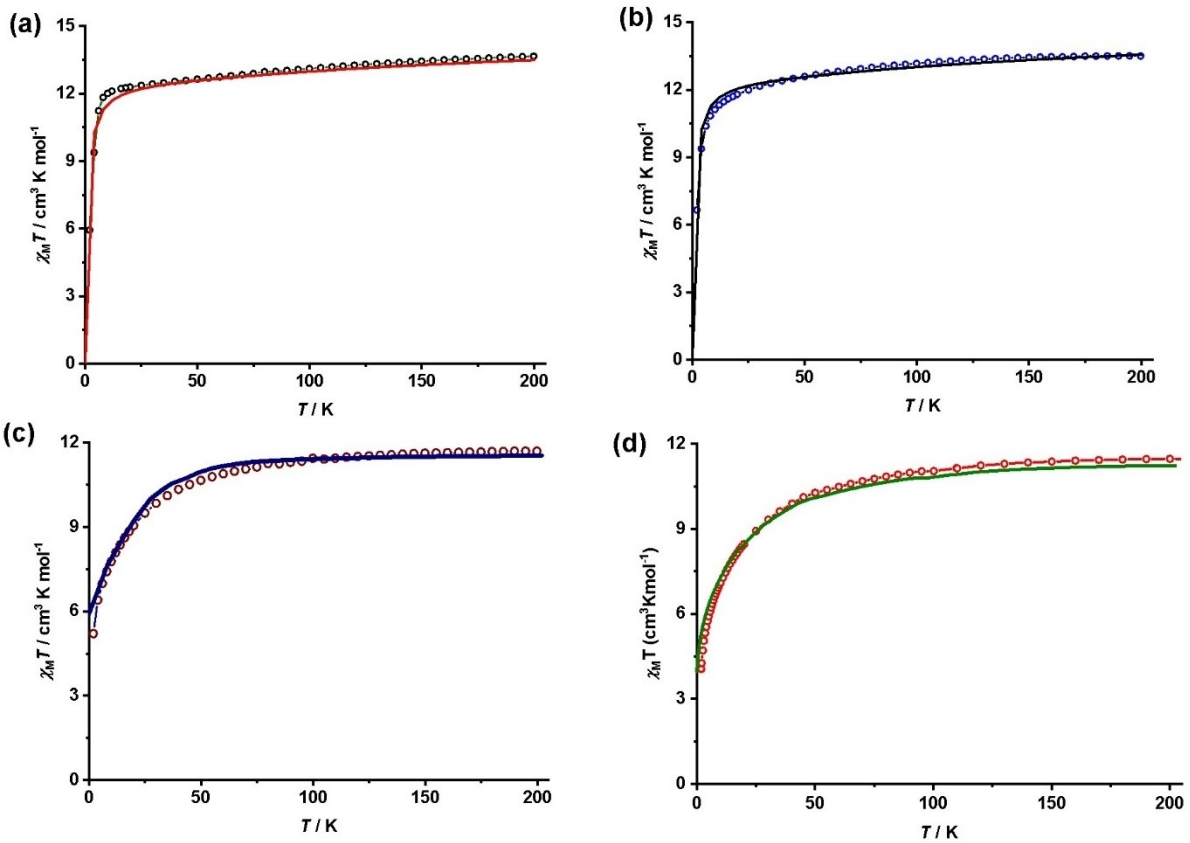

Figure 4. χ_MT versus T plots for (a) **1**, (b) **2**, (c) **3**, and (d) **4** and best fits derived from theoretical calculations (solid red lines). The intermolecular interactions are assumed to be −0.003, −0.01, −0.003, and −0.025 cm^{-1} for **1**–**4** in the calculations, respectively.

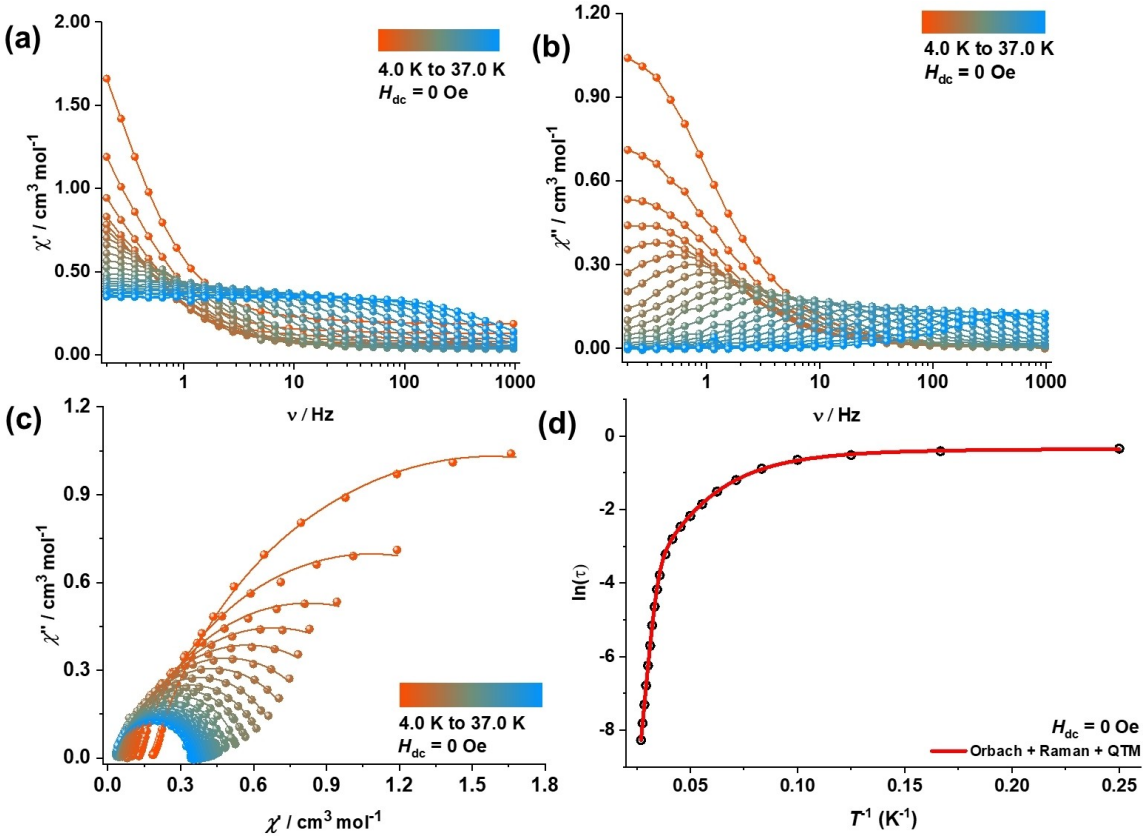

Figure 5. (a) In-phase and (b) out-of-phase component of frequency-dependent ac susceptibility measured in an oscillating ac field of 3.5 Oe and zero applied dc field for **1**. (c) Cole Cole plot for **1**. (d) Plot of the relaxation time obtained (logarithmic scale) versus T^{-1} obtained for **1** at zero field; the solid red line corresponds to the best fitting to the Orbach, Raman and QTM relaxation process for **1**.

effective barrier (U_{eff}) of 640 K and a pre-exponential factor (τ_0) of 7.95×10^{-12} s, indicating a very slow relaxation of magnetization, with n = 3.77, C = 8.88×10^{-5} s^{-1} K^{-n} and τ_{QTM} = 0.708 s (Figure 5d). The best fit for **2** yields U_{eff} of 491 K and a pre-exponential factor (τ_0) of 2×10^{-12} s, n = 3.88, C = 6.27×10^{-4} s^{-1} K^{-n} and τ_{QTM} = 0.852 s (Figure 6d). The curve deviates from linearity at 25 K.

$$\tau^{-1} = {\tau_{QTM}}^{-1} + AT + CT^{n} + {\tau_0}^{-1}\exp\left(-\frac{U_{eff}}{k_B T}\right) \quad (1)$$

To quench the QTM, frequency-dependent ac susceptibility measurements were also carried out in an optimized dc field of 1000 Oe for both **1** and **2**. The QTM was found to be suppressed for both **1** and **2** as seen from Figures S22 and S23, while the U_{eff} value remained almost unchanged at 640 K for **1** and 518 K for **2**.

No maxima were observed in the out-of-phase ac susceptibility measurements at zero field for **3** and **4**. However, upon application of a dc field of 1000 Oe, a clear maximum can be observed in the out-of-phase component of ac susceptibility for **3** within a temperature range of 1.8 K to 3.5 K (Figure S24b). The best fit for **3** revealed an energy barrier of 35.1 K and a pre-exponential factor of 8.58×10^{-9} s, indicating slow magnetic relaxation (Figure S24d) with C = 2.84 s^{-1} K^{-n} and n = 4.25. These values are also consistent with the Er(III)-based field-induced SIM complexes reported in the literature.[37] No maxima were observed in the out-of-phase component of ac susceptibility for **4**.

Variable-temperature zero field-cooled (ZFC) and field-cooled (FC) magnetization data were measured to determine the blocking temperature (T_B) for complexes **1** and **2** and the T_{irr} were obtained from the deviation of the field-cooled (FC) data with the ZFC curve (Figure 7). For compounds **1** and **2**, the magnetization blocking was attained at similar temperatures 6.5 K (**1**) and 6.0 K (**2**), indicating blocking of the molecular spin with a T_{irr} of 10.5 K and 8.2 K, respectively. In order to further investigate the SIM behaviour corresponding to the blocking of magnetization, field-dependent magnetization measurements were carried out at different temperatures at a sweep rate of 20 Oe/s (Figure S25). However, complexes **1** and **2** do not exhibit significant coercivity as observed in the case of $[L_2Dy(H_2O)_5][I]_3\cdot L_2\cdot(H_2O)$ (**A**).

Mechanism of Magnetisation Relaxation

To elucidate the relaxation mechanism and electronic structure of complexes **1**-**4**, we have performed ab initio CASSCF/RASSI-SO/SINGLE_ANISO calculations on their X-ray structures using

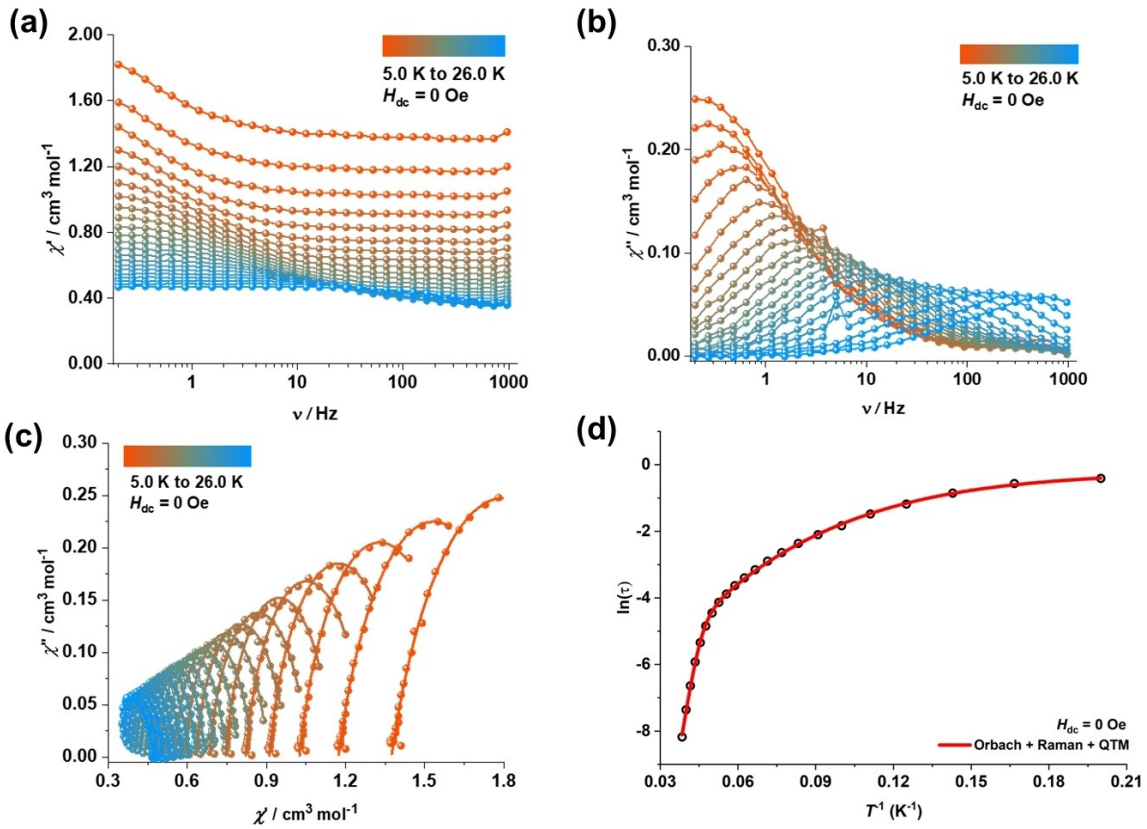

Figure 6. (a) In-phase and (b) out-of-phase component of frequency-dependent ac susceptibility measured in an oscillating ac field of 3.5 Oe and zero applied dc field for **2**. (c) Cole Cole plot for **2**. (d) Plot of the relaxation time obtained (logarithmic scale) versus T^{-1} obtained for **2** at zero field; the solid red line corresponds to the best fitting to the Orbach, Raman and QTM relaxation process for **2**.

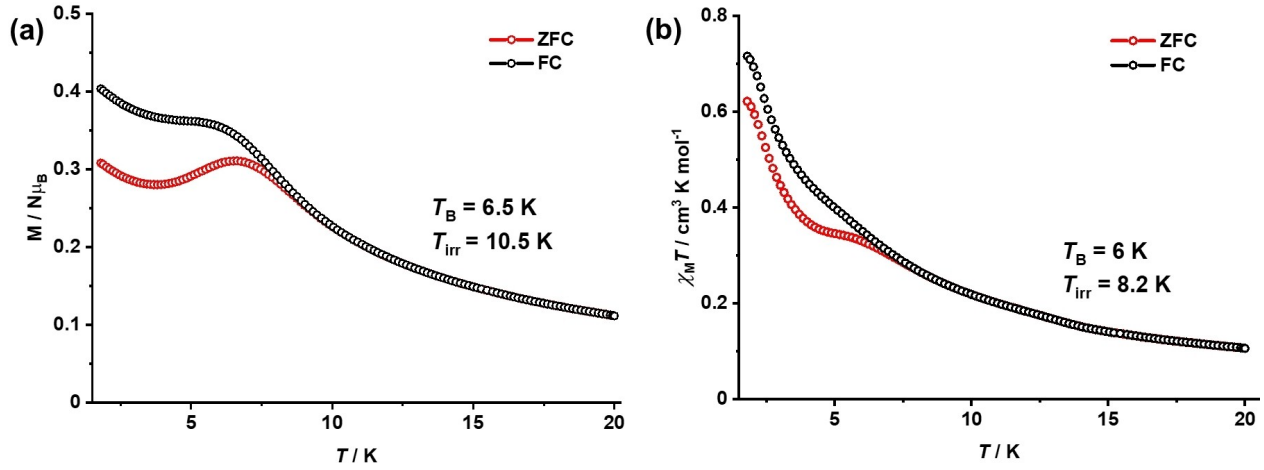

Figure 7. The plot of zero field-cooled (red) and field-cooled (black) magnetization vs. temperature for **1** and **2** collected with dc field of 1000 Oe at a sweep rate of 2 K/min.

the MOLCAS 8.2 program package[44] (see ESI for computational details). The computed g-tensors for the ground state KDs of complexes **1** and **2** reveal a purely Ising character (g_{xx}, $g_{yy} \approx 0$ and $g_{zz} = 19.935$, 19.916), with g_{zz} values close to ~20 and zero transverse components. This absence of transverse anisotropy indicates that the quantum tunnelling of magnetization (QTM) is quenched at this level. For complexes **1** and **2**, the ground state corresponds to a pure $m_J = |\pm 15/2\rangle$ state (Tables S13 and S14), with the g_{zz} axis aligning nearly along the pseudo-C_5 axis of the axial O–Dy–O bond (Figure 8). This is aligned with the Dy(III) complex with D_{5h} symmetry reported by us earlier (complex A).[37]

The first excited KD lies 435.2 K above the ground state for complex **1** and 425.8 K for complex **2** and is a pure $m_J = |\pm 13/2\rangle$ state (Tables S13 and S14) with negligible transverse anisotropy. This suggests that the first excited state KDs are strongly

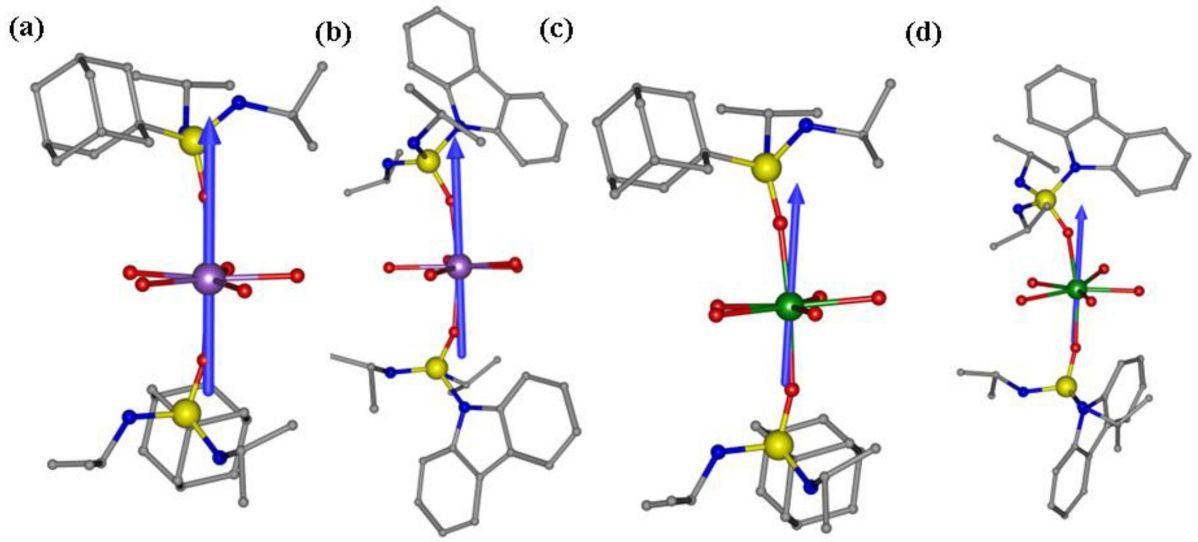

Figure 8. X-ray structures of complexes (a) **1**, (b) **2**, (c) **3** and (d) **4** along with the computed ground state g_{zz} axis (blue arrow). Dy, violet; Er, green; O, red; N, blue; P, yellow; C, grey. H atoms are excluded for clarity.

axial, reinforcing the quenching of QTM at this level. The g_{zz} orientation of this state aligns with the pseudo-C_5 axis, and the deviations with respect to this axis are noted as ~2.56° and 3.37° for complexes **1** and **2**, respectively. This alignment implies that relaxation is unlikely to occur via the first excited state.

The second excited KD, located 667.9 K above the ground state for complex **1** and 571.4 K for complex **2**, respectively, shows a significant transverse component (Tables S13 and S14). This state is an admixture of $m_J = |\pm 1/2\rangle$ and $m_J = |\pm 5/2\rangle$states (Tables S13 and S14) with the g_{zz} axis tilted by ~18.1° and 85.37° compared to the ground-state KD g_{zz} orientation. The substantial angular deviation and the presence of a transverse component suggest that the relaxation is more probable through this second excited state. Thus, the estimated barriers for relaxation are 667.2 K for complex **1** and 571.2 K for complex **2**. Apart from deviation from linearity, the addition of bulky adamantane (carbazole) ligand present in complex **1** (**2**), was found to have relatively strong Dy…H–C agostic interactions with a distance of 3.698 Å (3.376 Å) (Figure S28) which is also expected to infuse transverse anisotropy as shown in our earlier studies.[45–47] To examine the effect of Dy…H–C agostic interactions, we modelled an ideal D_{5h} molecule (**m1**) based on complex **1** (Figure S29). In this model, we manually adjusted the axial angle to 180° and set the equatorial bond angles to 72°, ensuring that all equatorial bond lengths were equal, as well as the axial bond lengths, with no agostic interactions present, as illustrated in Figure S29a. The calculated U_{cal} value for **m1** is 1679 K, with the relaxation occurring at the 3rd excited state, as shown in Figure S29b which apart from other established effects (stronger axial ligand field, weaker equatorial ligand field, O–Dy–O angle of 180° and ideal D_{5h} symmetry), agostic interaction is also one of the contributing reasons for the reduction in the barrier height.

In contrast to complexes **1** and **2**, the ground state KD of complexes **3** and **4** exhibits significant transverse anisotropy, with g-tensor components of $g_{xx} = 1.053$, $g_{yy} = 2.077$, $g_{zz} = 12.961$ for complex **3** and $g_{xx} = 1.394$, $g_{yy} = 1.192$, $g_{zz} = 11.861$ for complex **4**. This indicates significant QTM occurring at the ground state for both complexes. Additionally, significant mixing is observed between the ground state $m_J = |\pm 15/2\rangle$ and excited states $m_J = |\pm 11/2\rangle$, $m_J = |\pm 9/2\rangle$, $m_J = |\pm 7/2\rangle$, $m_J = |\pm 5/2\rangle$, $m_J = |\pm 3/2\rangle$, and $m_J = |\pm 1/2\rangle$ (Tables S16 and S17), suggesting considerable tunnelling at the ground KD level.

To gain further insights into the relaxation mechanism across all complexes (**1**–**4**), we analyzed the probable relaxation pathways and the computed energies of the first four KDs, as depicted in Figure 9 (a and b). For complexes **1** and **2**, the minimal transverse magnetic moments between the ground state and the first KDs indicate significant quenching of both QTM and TA-QTM. Conversely, TA-QTM via the second excited state is prominent in these complexes, as previously discussed in relation to transverse anisotropy. Additionally, the second excited state shows tunnelling probabilities of 1.2 μ_B and 2.6 μ_B for complexes **1** and **2**, respectively, supporting earlier observations.

For complexes **3** and **4**, quantum tunneling between the ground-state doublets is significant, with tunneling probabilities of 0.28 μ_B and 0.33 μ_B, respectively, suggesting a likely relaxation pathway shown in Figure 9 (c and d). This observation aligns with the absence of maxima in the out-of-phase ac signals at zero field.

To gain further insights into the relaxation mechanism, the crystal field parameters were computed (Table S18) using the equation implemented in the SINGLE_ANISO code $\widehat{H}_{CF} = \sum_{k=2,4,6} \sum_{q=-k}^{q=k} B_k^q \widehat{O}_k^q$ (here B_k^q is the crystal field parameter and $\widehat{O}_k^q$ is the Stevens operator respectively). The probability of observing QTM increases when the non-axial B_k^q terms (where

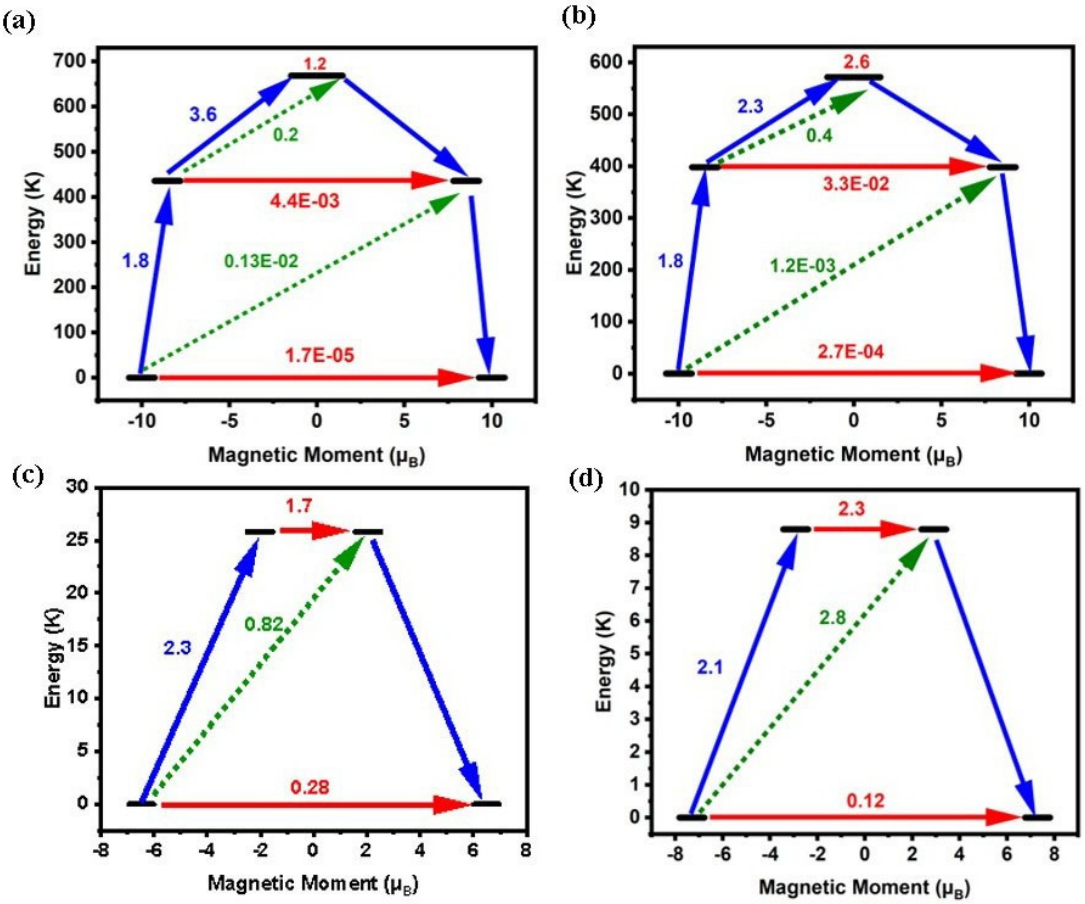

Figure 9. Magnetic relaxation in **1**–**4** (a–d) involve multiple pathways: Kramer's doublet (KD), QTM/TA-QTM via ground/excited states (red arrow), potential Orbach pathway (green arrow), and the most probable relaxation pathway (blue arrow). Associated numbers indicate mean absolute values of corresponding magnetic transition moment matrix elements.

$q \neq 0$ and $k = 2, 4, 6$) are larger than the axial terms (where $q = 0$) and $k = 2, 4, 6$). For complexes **1** and **2**, the axial terms are comparatively larger than the non-axial terms, suggesting minimal QTM. The large negative axial terms relative to the non-axial terms stabilize a high m_J value as the ground state. Conversely, for complexes **3** and **4**, the non-axial terms exceed the axial terms, promoting QTM between the ground-state KD.

Comparative Study of 1 and 2 with A

In perfect pentagonal bipyramidal D_{5h} systems, the axial O–Ln–O should be ideally linear. However, the axial trans bond angles of **1** and **2** having sterically hindered (Ad)P(O)(NH^{i}Pr)$_2$ (**L**^{1}) and (Cz)P(O)(NH^{i}Pr)$_2$ (**L**^{2}) as ligands, deviate from linearity to an extent of 173.7(1)° for **1** and 169.3(1)° for **2**, while the corresponding value for previously reported Dy-D_{5h} complex $[L_2Dy(H_2O)_5][I]_3 \cdot L_2 \cdot (H_2O)$ (**A**) where L = (^{t}BuPO(NH^{i}Pr)$_2$)][37] is 175.4°. While the deviation is small for compound **1**, it is substantial for compound **2**. This accounts for the observed significant decrease of U_{eff} value in **2**. The Dy···Dy separation in the lattice of **A** is 10.82 Å. However, the shortest distance between the two metal centres is increased to 14.28 Å in **1** and 11.94 Å in **3** which should have led to better magnetic properties due to lowered interactions between the metal centers. Nevertheless, the minimal change in U_{eff} for compound **1** relative to **A** can be attributed to a trade-off between the extended Dy···Dy distance and the distortion of the axial O–Dy–O bond. In other words, deviation of the axial bond angle from linearity does not lead to promising anisotropy barriers in complexes.[48] Table 2 and Figure 10 demonstrate

Table 2. Comparative table of structural parameters of **1** and **2** with **A**.

Bond angles, [°]/ Bond distances, [Å]	1	2	A
Trans O–Dy–O	173.7(1)	169.3(1)	175.4
Equatorial O–Dy–O	71.80(9)–72.5(2)	69.7(1)–74.37(6)	70.43(9)–73.52(1)
Dy1–O(P)	2.194(3)	2.221(2)	2.208, 2.203
Dy1–O (aqua)	2.357(3)	2.385(3)	2.35
Dy1–O (aqua)	2.345(4)	2.365(2)	2.36
Dy1–O (aqua)	2.405(4)	2.335(2)	2.37
Nearest Dy···Dy distance	14.2745(6)	11.9376(4)	10.82

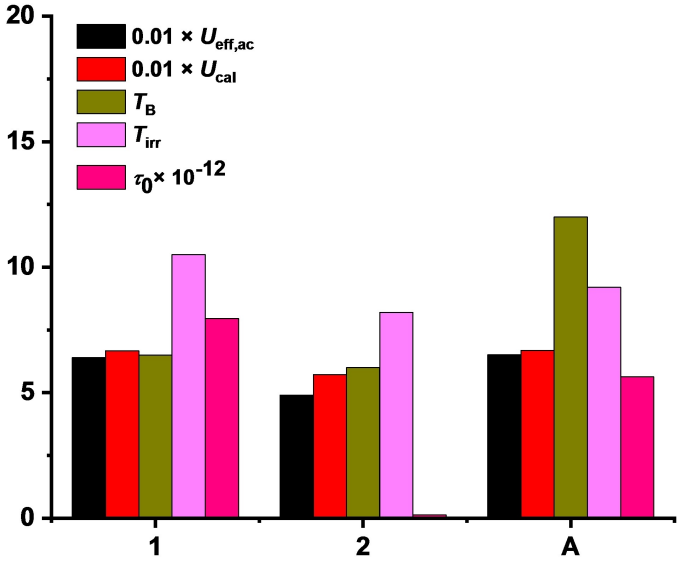

Figure 10. Comparative chart of the magnetic properties of SIMs **1** and **2** with **A**.

these differences. In addition to non-linearity, complex **1** (**2**) exhibits notable Dy…H–C agostic interactions 3.698 Å (3.376 Å) with the bulky adamantane (carbazole) ligand, as illustrated in Figure S28. This interaction is absent in complex **A**. The presence of these agostic interactions is anticipated to induce transverse anisotropy.

Experimental findings show that the U_{eff} Values for complexes **1**, **2**, and **A** follow the trend **A**>**1**>**2**. CASSCF calculations reveal that magnetization relaxation occurs in the 2nd excited state for all three complexes. The trend in U_{eff} is consistent with the trend observed for U_{cal}. To find out the origin of the increasing U_{cal} from **2**→**1**→**A**, we have estimated the crystal field parameters using the Hamiltonian $\widehat{H}_{CF} = \sum_{k=2,4,6} \sum_{q=-k}^{q=k} B_k^q \widehat{O}_k^q$ (here B_k^q is the crystal field parameter and $\widehat{O}_k^q$ is the Stevens operator respectively). The larger axial crystal field CF parameters (k = 2, 4, 6; q = 0) relative to the non-axial parameters (k = 2, 4, 6; q ≠ 0) indicate significant axiality in all three complexes (Table S**18**). The higher U_{cal} value for **A**, compared to **1** and **2**, is consistent with its larger axial B_k^q CF parameter. The computed LoProp charges also explain the increasing axiality from **2**→**1**→**A**. It is observed that **1** and **A** have similar LoProp charges on the axial atoms, while in complex **2**, the LoProp charge is lower compared to complexes **1** and **A**, as shown in Figure S**27**. It is well known that a higher negative charge on the axial donor atom leads to a higher barrier height, which is consistent with the experimental evidence.[16,28,49,50–53]

Conclusions

In conclusion, we have demonstrated the synthesis and magnetic properties of air-stable Dy(III) and Er(III)-based isostructural pseudo-D_{5h} single-ion magnets (SIMs). This study emphasizes the critical role of the central metal ion's geometry, particularly the linearity of the O–Dy–O bond, in achieving high anisotropic barriers within these systems. Comparative analysis of complexes **1** and **2** reveals that modifying the immediate environment around the coordinating P–O bond through P–N substitution in **2** diminishes the effective anisotropy barrier (U_{eff}). Furthermore, while intermetallic distances increase in both compounds relative to the phosphonamide complex **A**, larger tilting of the axial ligands in **2** with respect to **1**, leads to increased transverse anisotropy and thereby compromised U_{eff} values and blocking temperatures in the order **A**>**1**>**2** for the complexes. In addition to the non-linearity, the bulky adamantane (carbazole) ligand in complex **1** (**2**) forms relatively strong Dy…H–C agostic interactions. These interactions contribute to higher transverse anisotropy in **1** and **2** compared to **A**, resulting in a higher barrier height for **A** followed by **1** and then **2**. The ab initio CASSCF/RASSI-SO/SINGLE – ANISO calculations support the experimental findings, showing that the higher U_{cal} obtained for **A** is due to its larger axial crystal field parameter. The computed LoProp charges explain the increasing axiality from **2** to **1** to **A**, with complexes **1** and **A** having similar axial charges, while **2** has a lower charge. This aligns with the established understanding that a higher negative charge on the axial donor atom leads to a higher barrier height, consistent with experimental results.

Experimental Section

Instruments and Methods

All the reactions were performed under ambient reaction conditions. Fourier-transform infrared spectra were recorded on a PerkinElmer Spectrum One spectrometer using KBr diluted pellets in the frequency range 4000–400 cm^{-1}. Melting points were measured in glass capillaries and are reported uncorrected. ESI-MS measurements were performed on an Agilent 6545 LC/Q-TOF and Bruker Maxis Impact electrospray mass spectrometers. Elemental analyses were carried out using vacuum dried samples (at times with variable amounts of lattice solvent molecule) using a VarioMicro Cube (Elementar Analysensysteme GmbH) microanalyzer. Powder X-ray diffraction studies were recorded on a Rigaku SmartLab powder X-ray diffractometer using Cu–Kα radiation (λ = 1.54190 Å). NMR spectral measurements were conducted using Bruker Avance DPX-400 MHz spectrometers in solution. The magnetic properties of the polycrystalline samples were measured using a Quantum Design MPMS-XL SQUID magnetometer equipped with a 7 T magnet in the temperature range of 2–200 K. The data were corrected for background contribution and consequently Pascal's constants. Alternating current (ac) susceptibility measurements were performed in the same machine using an oscillating ac field of 3.5 Oe at indicated frequencies between 0.1 and 1500 Hz.

Materials

Commercial-grade solvents were purified and dried by employing conventional procedures.[54] Adamantyl bromide (Merck), n-butyl lithium (Spectrochem), PCl_3 (Spectrochem), anhydrous $AlCl_3$ (Avra), $POCl_3$ (Spectrochem), concentrated HI (Merck), and carbazole (Merck) were procured from commercial sources and used as such. Isopropyl amine (Merck) was dried over KOH prior to the use following literature methods.[54] Lanthanide iodides were prepared

from Ln(III) oxides (Alfa Aesar) and hydroiodic acid. Ligand L^1 was synthesized starting from $AdP(O)Cl_2$ (details in ESI).[38]

Single crystal X-Ray Crystallography

For unit cell determination and diffraction intensity data collection, a suitabletatabltabta crystal of each compound was mounted on a Bruker D8 QUEST single crystal diffractometer equipped with a Mo–Kα radiation source (λ = 0.71073 Å). Rigaku CrysAlisPro software package was used for data integration and indexing.[55] Using Olex2,[56] the structure was solved employing ShelXT[57] structure solution programme utilizing intrinsic phasing. The structures were refined by ShelXL[58] using least squares minimization. Anisotropic refinement was used for all non-hydrogen atoms. Details of data collection, unit cell dimensions, refinement, and final residual values are listed in Table S3. All figures were created with Diamond 3.2 software.[59] CCDC reference numbers 2380632 (**1**), 2380633 (**2**), 2380634 (**3**), 2380635 (**4**) and 2380636 (L^2) contain supplementary crystallographic data, which can be obtained free of charge from the Cambridge Crystallographic Data Centre. Metal coordination geometry analyses were performed using SHAPE2.1.[43] Severe positional disorder in one of the two lattice dichloromethane molecules in the asymmetric part of the unit cell of **4** precluded its precise positional determination and refinement. Hence, this molecule was masked by using solvent mask as implemented in Olex2. The crystal data presented in Table S3 also excludes this masked dichloromethane in the molecular formula.

Synthesis and Characterization of $(Cz)P(O)(NH^iPr)_2$ (L^2)

3.34 g (20 mmol) of carbazole was dissolved in 60 mL of dry THF in a Schlenk flask equipped with a magnetic stir bar. n-Butyl lithium (15 mL, 26 mmol) was added to the above solution at −78 °C (liquid N_2/Acetone bath) followed by dropwise addition of $POCl_3$ (1.9 mL, 20 mmol) to the resulting mixture with constant stirring. The stirring stops as the reaction mixture reaches room temperature due to the formation of a viscous liquid which then solidifies over time upon pumping off the solvent. The solid $(Cz)P(O)Cl_2$ obtained was then dissolved in toluene and cooled down to 0 °C. To this, isopropylamine (4 mL, 40 mmol) was added dropwise and the reaction was allowed to reflux for 12 hours. Isopropyl ammonium chloride precipitates out from the reaction mixture as a white solid which was eliminated from the reaction mixture by Schlenk filtration. The crude $(Cz)P(O)(NH^iPr)_2$ obtained was then washed repeatedly with cold toluene and recrystallized from methanol at ambient conditions. Yield: 5.5 g (83 %). Mp.: 210 °C. ESI-MS for Mr $C_{18}H_{24}N_3OP$: m/z 330.18 $(M+H)^+$, IR (KBr, cm^{-1}): 3268 (N–H str), 2865 (C–H str), 1598 (N–H bending), 1204 (P=O), 983 (P–N). ^{31}P NMR (202 MHz, $CDCl_3$): 4.92 ppm (s, P=O); ^1H NMR (400 MHz, $CDCl_3$) δ (ppm): 8.17 (d, $^3J_{H,H}$ = 8.44 Hz, 2H), 8.01 (d, $^3J_{H,H}$ = 7.84 Hz, 2H), 7.42 (t, $^3J_{H,H}$ = 7.00 Hz, ^1H), 7.31 (t, $^3J_{H,H}$ = 7.13 Hz, ^1H), 3.47 (sept, $^3J_{H,H}$ = 6.51 Hz, 2H), 1.19 (d, $^3J_{H,H}$ = 6.48 Hz, 6H), 0.89 (d, $^3J_{H,H}$ = 6.48 Hz, 6H); ^{13}C NMR (101 MHz, $CDCl_3$) δ (ppm): 141.30, 126.34, 126.04, 121.49, 129.74, 114.86, 43.76, 25.78, 25.71, 25.25, 25.19.

Synthesis of $[L^1{}_2Dy(H_2O)_5][I]_3 \cdot L^1{}_2 \cdot (CH_2Cl_2)$ (1)

To a pink coloured solution of hydrated $DyI_3 \cdot xH_2O$ (0.1 mmol, 54 mg) in dichloromethane (15 mL), L^1 (0.2 mmol, 60 mg) was added and stirred for an hour at room temperature. This produced a clear yellow solution which was stirred at 60 °C for 6 hours before cooling down to room temperature. The resulting solution was then filtered and kept for crystallization at ambient temperature. Yellow block-shaped crystals of **1** were obtained over a period of one week through slow evaporation of the solvent. Yield: 0.046 g (48 %, based on ligand), Mp.: 140 °C, Anal. (Calcd) for $C_{65}H_{136}DyN_8O_9P_4Cl_2I_3$ (Mr 1911.85) C: 40.46 (40.84) H: 7.36 (7.17) N: 5.40 (5.86). FT-IR (as KBr diluted disc, cm^{-1}): 3412 (O–H str), 3316 (N–H str), 2968, 2906 (C–H str), 2850, 2299, 1641 (N–H bending), 1421, 1100 (P=O), 1079 (P–N bending), 734, 568.

Synthesis of $[L^2{}_2Dy(H_2O)_5][I]_3 \cdot L^2{}_2 \cdot (CH_2Cl_2)_2$ (2)

To a pink coloured solution of hydrated $DyI_3 \cdot xH_2O$ (0.1 mmol, 54 mg) in dichloromethane (15 mL), L^2 (0.4 mmol, 138 mg) was added and stirred for an hour at room temperature. This produced a clear yellow solution which was stirred at 60 °C for 4 hours before cooling down to room temperature. The solution was then filtered and kept for crystallization at ambient temperature. Yellow block-shaped crystals of **2** were obtained over a period of three to four weeks through slow evaporation of the solvent. Yield: 0.126 g (63 %, based on ligand), Mp.: > 250 °C; Anal. (Calcd.) for $C_{72}H_{106}DyI_3N_{12}O_9P_4$ (vacuum dried sample) (Mr 1950.82) C: 45.20 (44.33) H: 5.21 (5.48) N: 8.12 (8.62). FT-IR (KBr, cm^{-1}): 3361 (O–H str), 3299 (N–H str), 3056, 2972, 2931 (C–H str), 2876, 2848, 1603 (N–H bending), 1455, 1424, 1384, 1366, 1315, 1131 (P=O), 1098, 1054 (P–N bending), 732, 566.

Synthesis of $[L^1{}_2Er(H_2O)_5][I]_3 \cdot L^1{}_2 \cdot (CH_2Cl_2)$ (3)

Complex **3** was synthesized following the same procedure as used for complex **1**, except that $ErI_3 \cdot xH_2O$ (0.1 mmol, 55 mg) was substituted for $DyI_3 \cdot xH_2O$. Yield: 0.051 g (53 %, based on ligand), Mp.: 145 °C; Anal. (Calcd) for $C_{65}H_{136}ErN_8O_9P_4Cl_2I_3$ (Mr 1913.52) C: 40.23 (40.73) H: 7.38 (7.15) N 5.48 (5.85). FT-IR (as KBr diluted disc, cm^{-1}): 3423 (O–H str), 3291 (N–H str), 2968, 2870 (C–H str), 1619 (N–H bending), 1476, 1423, 1115 (P=O), 1025 (P–N bending), 731, 654, 545.

Synthesis of $[L^2{}_2Er(H_2O)_5][I]_3 \cdot L^2{}_2 \cdot (CH_2Cl_2)_2$ (4)

Complex **4** was synthesized following the same procedure as used for complex **2**, except that $ErI_3 \cdot xH_2O$ (0.1 mmol, 55 mg) was substituted for $DyI_3 \cdot xH_2O$. Yield: 0.138 g (65 %, based on ligand), Mp.: > 250 °C; Anal. (Calcd.) for $C_{72}H_{106}ErI_3N_{12}O_9P_4$ (vacuum dried sample): (Mr 1955.58) C: 45.90 (44.22) H: 5.90 (5.46) N: 7.85 (8.60). FT-IR (KBr, cm^{-1}): 3410 (O–H str), 3303 (N–H str.), 3296, 3060, 2975, 2957, 2930 (C–H str), 2872, 1625 (N–H bending), 1585, 1517, 1464, 1428, 1379, 1161, 1121 (P=O), 1054, 1028, 1000 (P–N bending), 869, 850, 807, 727, and 612.

Supporting Information

Crystallographic details, spectral characterization and additional figures and tables are available free of charge. CCDC reference numbers 2380632 (**1**), 2380633 (**2**), 2380634 (**3**), 2380635 (**4**) and 2380636 (L^2) contain the supplementary crystallographic data for this paper.

Acknowledgements

R. M. acknowledges financial support by SERB, New Delhi through CRG/2022/002406 and SB/S2/JCB-85/2014 and by MoE through SPARC/2019-2020/P1677/SL. A. G. and R. R. thank Prime Minister's Research Fellowship (PMRF) for a research fellowship.

S. K. G. thanks the Alexander von Humboldt foundation for a research fellowship and IIT Delhi for the seed grant. The purchase of the SQUID magnetometer was supported by the DFG (project number INST 186/1329-1 FUGG) and the Niedersächsische Ministerium für Wissenschaft und Kultur (MWK). The authors thank the MoE IoE-funded central facilities and SAIF, IIT Bombay for characterization data. G. R. thanks SERB for funding (SB/SJF/2019-20/12; CRG/2022/001697).

Conflict of Interests

The authors declare no conflict of interest.

Data Availability Statement

The data that support the findings of this study are available in the supplementary material of this article.

Keywords: Single molecule magnets (SMM) · phosphonamides, pseudo-D_{5h} · lanthanide complexes · axial anisotropy.

[1] C. P. Chen, C.-Y. Zhang, *Inf. Sci.* **2014**, *275*, 314–347.
[2] D. Gatteschi, R. Sessoli, J. Villain, *Molecular nanomagnets, Vol. 5*, Oxford University Press, USA, **2006**.
[3] M. Ganzhorn, S. Klyatskaya, M. Ruben, W. Wernsdorfer, *Nat. Nanotechnol.* **2013**, *8*, 165–169.
[4] E. M. Pineda, T. Komeda, K. Katoh, M. Yamashita, M. Ruben, *Dalton Trans.* **2016**, *45*, 18417–18433.
[5] R. Sessoli, D. Gatteschi, A. Caneschi, M. Novak, *Nature* **1993**, *365*, 141–143.
[6] M. Mannini, F. Pineider, P. Sainctavit, C. Danieli, E. Otero, C. Sciancalepore, A. M. Talarico, M.-A. Arrio, A. Cornia, D. Gatteschi, *Nat. Mater.* **2009**, *8*, 194–197.
[7] M. Urdampilleta, S. Klyatskaya, J.-P. Cleuziou, M. Ruben, W. Wernsdorfer, *Nat. Mater.* **2011**, *10*, 502–506.
[8] L. Bogani, W. Wernsdorfer, *Nat. Mater.* **2008**, *7*, 179–186.
[9] M. Mannini, F. Pineider, C. Danieli, F. Totti, L. Sorace, P. Sainctavit, M.-A. Arrio, E. Otero, L. Joly, J. C. Cezar, *Nature* **2010**, *468*, 417–421.
[10] D. Aravena, E. Ruiz, *Dalton Trans.* **2020**, *49*, 9916–9928.
[11] A. Caneschi, D. Gatteschi, R. Sessoli, A. L. Barra, L. C. Brunel, M. Guillot, *J. Am. Chem. Soc.* **1991**, *113*, 5873–5874.
[12] N. Ishikawa, M. Sugita, T. Ishikawa, S.-y. Koshihara, Y. Kaizu, *J. Am. Chem. Soc.* **2003**, *125*, 8694–8695.
[13] S. K. Gupta, R. Murugavel, *Chem. Commun.* **2018**, *54*, 3685–3696.
[14] A. J. Brown, D. Pinkowicz, M. R. Saber, K. R. Dunbar, *Angew. Chem.* **2015**, *127*, 5962–5966.
[15] C. A. Gould, K. R. McClain, J. M. Yu, T. J. Groshens, F. Furche, B. G. Harvey, J. R. Long, *J. Am. Chem. Soc.* **2019**, *141*, 12967–12973.
[16] Y. S. Ding, N. F. Chilton, R. E. Winpenny, Y. Z. Zheng, *Angew. Chem. Int. Ed.* **2016**, *55*, 16071–16074.
[17] R. J. Blagg, L. Ungur, F. Tuna, J. Speak, P. Comar, D. Collison, W. Wernsdorfer, E. J. McInnes, L. F. Chibotaru, R. E. Winpenny, *Nat. Chem.* **2013**, *5*, 673–678.
[18] L. Sorace, C. Benelli, D. Gatteschi, *Chem. Soc. Rev.* **2011**, *40*, 3092–3104.
[19] A. Borah, R. Murugavel, *Coord. Chem. Rev.* **2022**, *453*, 214288.
[20] A. Borah, S. Dey, S. K. Gupta, M. G. Walawalkar, G. Rajaraman, R. Murugavel, *Chem. Commun.* **2020**, *56*, 11879–11882.
[21] S. K. Gupta, S. Shanmugan, T. Rajeshkumar, A. Borah, M. Damjanović, M. Schulze, W. Wernsdorfer, G. Rajaraman, R. Murugavel, *Dalton Trans.* **2019**, *48*, 15928–15935.
[22] A. Borah, S. Dey, S. K. Gupta, G. Rajaraman, R. Murugavel, *Dalton Trans.* **2023**, *52*, 8943–8955.
[23] N. F. Chilton, C. A. Goodwin, D. P. Mills, R. E. Winpenny, *Chem. Commun.* **2015**, *51*, 101–103.
[24] G. Cucinotta, M. Perfetti, J. Luzon, M. Etienne, P. E. Car, A. Caneschi, G. Calvez, K. Bernot, R. Sessoli, *Angew. Chem. Int. Ed.* **2012**, *51*, 1606–1610.
[25] F. Tuna, C. A. Smith, M. Bodensteiner, L. Ungur, L. F. Chibotaru, E. J. McInnes, R. E. Winpenny, D. Collison, R. A. Layfield, *Angew. Chem.* **2012**, *124*, 7082–7086.
[26] C. A. Goodwin, F. Ortu, D. Reta, N. F. Chilton, D. P. Mills, *Nature* **2017**, *548*, 439–442.
[27] B. M. Day, F. S. Guo, S. R. Giblin, A. Sekiguchi, A. Mansikkamäki, R. A. Layfield, *Chem. Eur. J.* **2018**, *24*, 16779–16782.
[28] J. D. Rinehart, J. R. Long, *Chem. Sci.* **2011**, *2*, 2078–2085.
[29] L. Ungur, L. F. Chibotaru, *Phys. Chem. Chem. Phys.* **2011**, *13*, 20086–20090.
[30] S. K. Singh, T. Gupta, G. Rajaraman, *Inorg. Chem.* **2014**, *53*, 10835–10845.
[31] S.-D. Jiang, S.-S. Liu, L.-N. Zhou, B.-W. Wang, Z.-M. Wang, S. Gao, *Inorg. Chem.* **2012**, *51*, 3079–3087.
[32] S.-S. Liu, J. W. Ziller, Y.-Q. Zhang, B.-W. Wang, W. J. Evans, S. Gao, *Chem. Commun.* **2014**, *50*, 11418–11420.
[33] M. He, F.-S. Guo, J. Tang, A. Mansikkamäki, R. A. Layfield, *Chem. Commun.* **2021**, *57*, 6396–6399.
[34] J. Emerson-King, G. K. Gransbury, G. F. Whitehead, I. J. Vitorica-Yrezabal, M. Rouzières, R. Clérac, N. F. Chilton, D. P. Mills, *J. Am. Chem. Soc.* **2024**, *146*, 3331–3342.
[35] F.-S. Guo, B. M. Day, Y.-C. Chen, M.-L. Tong, A. Mansikkamäki, R. A. Layfield, *Science* **2018**, *362*, 1400–1403.
[36] C. A. Gould, K. R. McClain, D. Reta, J. G. Kragskow, D. A. Marchiori, E. Lachman, E.-S. Choi, J. G. Analytis, R. D. Britt, N. F. Chilton, *Science* **2022**, *375*, 198–202.
[37] S. K. Gupta, T. Rajeshkumar, G. Rajaraman, R. Murugavel, *Chem. Sci.* **2016**, *7*, 5181–5191.
[38] C. Healy, F. W. Steuber, P. Wix, L. K. Macreadie, A. C. Kathalikkattil, W. Schmitt, *Dalton Trans.* **2019**, *48*, 3018–3027.
[39] R. Murugavel, R. Pothiraja, *New J. Chem.* **2003**, *27*, 968–974.
[40] K. Gholivand, Z. Shariatinia, N. Oroujzadeh, *Heteroat. Chem.* **2013**, *24*, 404–412.
[41] S. K. Gupta, T. Rajeshkumar, G. Rajaraman, R. Murugavel, *Chem. Commun.* **2016**, *52*, 7168–7171.
[42] S. K. Gupta, T. Rajeshkumar, G. Rajaraman, R. Murugavel, *Dalton Trans.* **2018**, *47*, 357–366.
[43] M. Llunell, D. Casanova, J. Cirera, J. M. Bofill, P. Alemany, S. Alvarez, M. Pinsky, D. Avnir, **2013**, SHAPE (Version 2.1).
[44] F. Aquilante, J. Autschbach, R. K. Carlson, L. F. Chibotaru, M. G. Delcey, L. De Vico, I. Fdez. Galván, N. Ferré, L. M. Frutos, L. Gagliardi, Molcas 8: New capabilities for multiconfigurational quantum chemical calculations across the periodic table, **2016**.
[45] A. Swain, R. K. Tiwari, M. Khatua, G. Rajaraman, *Inorg. Chem.* **2023**, *62*, 9552–9562.
[46] T. Gupta, G. Velmurugan, T. Rajeshkumar, G. Rajaraman, *J. Chem. Sci.* **2016**, *128*, 1615–1630.
[47] S. Dey, G. Velmurugan, G. Rajaraman, *Dalton Trans.* **2019**, *48*, 8976–8988.
[48] M. S. Norre, C. Gao, S. Dey, S. K. Gupta, A. Borah, R. Murugavel, G. Rajaraman, J. Overgaard, *Inorg. Chem.* **2019**, *59*, 717–729.
[49] Y. S. Ding, T. Han, Y. Q. Zhai, D. Reta, N. F. Chilton, R. E. Winpenny, Y. Z. Zheng, *Chem. Eur. J.* **2020**, *26*, 5893–5902.
[50] E. Regincós Martí, A. B. Canaj, T. Sharma, A. Celmina, C. Wilson, G. Rajaraman, M. Murrie, *Inorg. Chem.* **2022**, *61*, 9906–9917.
[51] N. Monni, S. Dey, V. García-López, M. Oggianu, J. J. Baldoví, M. L. Mercuri, M. Clemente-León, E. Coronado, *Inorg. Chem. Front.* **2024**, *11*, 5913–5923.
[52] A. Sarkar, G. Rajaraman, *Chem. Sci.* **2020**, *11*, 10324–10330.
[53] J. Liu, Y.-C. Chen, J.-L. Liu, V. Vieru, L. Ungur, J.-H. Jia, L. F. Chibotaru, Y. Lan, W. Wernsdorfer, S. Gao, *J. Am. Chem. Soc.* **2016**, *138*, 5441–5450.
[54] D. D. Perrin, W. L. Armarego, *Purification of laboratory chemicals*, 3rd Edition, Pergamon Press, Oxford, **1988**.
[55] CrysAlisPRO; Rigaku Oxford Diffraction Ltd: Yarnton, Oxfordshire, England.
[56] G. M. Sheldrick, *Acta Crystallogr. Sect. A* **2008**, *64*, 112–122.
[57] G. M. Sheldrick, *Acta Crystallogr. Sect. C* **2015**, *71*, 3–8.
[58] G. M. Sheldrick, *Acta Crystallogr. Sect. A* **2015**, *71*, 3–8.
[59] Diamond – Crystal and Molecular Structure Visualization, Crystal Impact – Dr. H. Putz & Dr. K. Brandenburg GbR, Kreuzherrenstr. 2008, 2102, 53227 Bonn, Germany.
[60] S. K. Gupta, S. Dey, T. Rajeshkumar, G. Rajaraman, R. Murugavel, *Chem. Eur. J.* **2022**, *28*, e202103585.

[61] Y.-C. Chen, J.-L. Liu, L. Ungur, J. Liu, Q.-W. Li, L.-F. Wang, Z.-P. Ni, L. F. Chibotaru, X.-M. Chen, M.-L. Tong, *J. Am. Chem. Soc.* **2016**, *138*, 2829–2837.
[62] Y. C. Chen, J. L. Liu, Y. Lan, Z. Q. Zhong, A. Mansikkamäki, L. Ungur, Q. W. Li, J. H. Jia, L. F. Chibotaru, J. B. Han, W. Wernsdorfer, *Chem. Eur. J.* **2017**, *23*, 5708–5715.
[63] A. B. Canaj, M. K. Singh, C. Wilson, G. Rajaraman, M. Murrie, *Chem. Commun.* **2018**, *54*, 8273–8276.
[64] I. F. Díaz-Ortega, J. M. Herrera, S. Dey, H. Nojiri, G. Rajaraman, E. Colacio, *Inorg. Chem. Front.* **2020**, *7*, 689–699.

Manuscript received: October 24, 2024
Revised manuscript received: December 27, 2024
Accepted manuscript online: January 2, 2025
Version of record online: January 22, 2025